Ultrafast molecular motor driven nanoseparation and biosensing

Mercy Lard [a,1], Lasse ten Siethoff [b,1], Saroj Kumar [b], Malin Persson [b], Geertruy te Kronnie [c], Heiner Linke [a], Alf Månsson [b,*]

[a] The Nanometer Structure Consortium (nmC@LU), Division of Solid State Physics, Lund University, SE-221 00 Lund, Sweden
[b] Department of Chemistry and Biomedical Sciences, Linnaeus University, SE-391 82 Kalmar, Sweden
[c] Department of Women's and Children's Health, University of Padova, 35131 Padova, Italy

A B S T R A C T

Portable biosensor systems would benefit from reduced dependency on external power supplies as well as from further miniaturization and increased detection rate. Systems built around self-propelled biological molecular motors and cytoskeletal filaments hold significant promise in these regards as they are built from nanoscale components that enable nanoseparation independent of fluidic pumping. Previously reported microtubule-kinesin based devices are slow, however, compared to several existing biosensor systems. Here we demonstrate that this speed limitation can be overcome by using the faster actomyosin motor system. Moreover, due to lower flexural rigidity of the actin filaments, smaller features can be achieved compared to microtubule-based systems, enabling further miniaturization. Using a device designed through optimization by Monte Carlo simulations, we demonstrate extensive myosin driven enrichment of actin filaments on a detector area of less than 10 μm^2, with a concentration half-time of approximately 40 s. We also show accumulation of model analyte (streptavidin at nanomolar concentration in nanoliter effective volume) detecting increased fluorescence intensity within seconds after initiation of motor-driven transportation from capture regions. We discuss further optimizations of the system and incorporation into a complete biosensing workflow.

© 2013 Elsevier B.V. All rights reserved.

1. Introduction

Portable biosensors with increased sensitivity, rate of detection and capacity for multiplexing (Giljohann and Mirkin, 2009; Jokerst et al., 2010; Ng et al., 2010) are of appreciable interest for improved point-of-care medical diagnostics and related applications. Realizations of high-performance devices have been proposed using nanostructures (Giljohann and Mirkin, 2009; Lee et al., 2004; Nam et al., 2003; Zhang et al., 2005a, 2005b) combined with microfluidics/nanofluidics for specific concentration of analytes from a complex sample mixture (Jokerst et al., 2010; Ng et al., 2010; Whitesides, 2006). However, particularly nanofluidics requires strong driving forces for liquid transport (Månsson et al., 2005), and depends on bulky accessory equipment such as pumps and various control devices (Jokerst et al., 2010; Whitesides, 2006). One way to circumvent these problems would be to use Adenosine-5'-triphosphate (ATP)-driven biological molecular motors for separation and concentration of analyte molecules on detector sites (Fischer et al., 2009; Korten et al., 2010;

Lin et al., 2008). In this process, the analyte molecules are linked to motor-propelled cytoskeletal filament shuttles (Bachand et al., 2006; Brunner et al., 2007; Hess et al., 2001; Månsson et al., 2004; Ramachandran et al., 2006) and guided on nanopatterned surfaces (Ashikari et al., 2012; Bunk et al., 2005b; Byun et al., 2007; Hess et al., 2001; Nicolau et al., 1999; Sundberg et al., 2006b; Suzuki et al., 1997) to the desired sites. In addition to advantages over microfluidics driven separation, the actual detection of analytes may be achieved in unique ways using motor driven devices e.g. by the actual observation of cotransportation of filaments and analytes (e.g. Korten et al., 2013). One automated approach that combines this unique biosensing principle with separation is transportation of analytes to a pre-determined detection site that can be readily reached only by motor driven transportation. Whereas proof-of-principle devices of this type have been reported using the microtubule-kinesin motor system (Fischer et al., 2009; Lin et al., 2008) these devices have shown orders of magnitude, lower rates of detection than other high-sensitivity methods (Georganopoulou et al., 2005; Mulvaney et al., 2009; Nam et al., 2003; Rissin et al., 2010).

A way to overcome the limitations in speed may be to use myosin-propelled actin filaments that are ten-fold faster than kinesin-propelled microtubules. This idea is supported by the recent demonstration of consistent heavy meromyosin (HMM)

* Corresponding author. Tel.: +46 480 446 243; fax: +46 480 446 262.
E-mail address: alf.mansson@lnu.se (A. Månsson).
[1] These authors contributed equally to this work.

driven transportation of a large number of antibody–antigen complexes (Kumar et al., 2012). Moreover, the low flexural rigidity (Vikhorev et al., 2008a) of actin filaments compared to microtubules would enable more extensive miniaturization that may also contribute to further increased detection rate. We thus hypothesize that actin filaments can be concentrated by myosin driven transport, orders of magnitude faster than in previous motor driven devices (Fischer et al., 2009; Lin et al., 2008). Moreover, we expect that the use of actin filaments allows further miniaturization, e.g. of the detector site, with favorable effects on the signal/noise ratio (Katira and Hess, 2010b). With the aim to test these ideas, we first present experiments using a generic concentrator device to validate a Monte-Carlo simulation approach (Nitta et al., 2006, 2008) that is then used for rational design of an optimized device. Experiments employing the latter device showed rates of concentration that were nearly two orders of magnitude faster than in earlier motor-driven devices but also faster than key amplification steps in non-motor based diagnostic tests (Georganopoulou et al., 2005; Nam et al., 2003). Moreover, further miniaturization compared to microtubule-kinesin devices, allowed actin filament capture and subsequent guidance to detector site of less than 10 μm^2 total area. We discuss further optimizations and the most effective incorporation of the tested device into complete workflows for high-sensitivity detection of analytes in, for example, clinical diagnostics and environmental monitoring.

2. Materials and methods

2.1. Nanostructuring and surface preparation

An SiO_2 layer of 825 nm thickness was grown by wet thermal oxidation on a Si wafer followed by covering with lift-off resist (LOR 0.7A; Microchem Corporation, Newton, MA, USA) using spin coating at 1500 RPM for 30 s and subsequent baking at 180 °C for 15 min on a hot plate. Next, polymethylmethacrylate, (PMMA 950A5; Microchem Corporation, Newton, MA, USA) was spin-coated on top at 6000 RPM for 60 s, followed by baking at 160 °C for 15 min. This PMMA resist layer was exposed by electron-beam lithography (EBL; Raith 150, Dortmund, Germany) giving top line widths of approximately 185 nm in the PMMA. The PMMA was then developed with methyl isobutyl ketone and isopropanol (MIBK:IPA; Merck KGaA, Darmstadt, Germany) at a ratio of 1:3 for 1 min, followed by rinsing with IPA for 30 s. Next, the sample was subjected to O_2 plasma ashing in a Plasma Preen at 5 mBar for 15 s. Then, the LOR layer was etched with MF-319:H_2O (Microposit MF-319 Developer, Rohm and Haas Electronic Materials, Coventry, UK) in the ratio 1:1 for 4 min and rinsed with H_2O for 30 s to halt etching. The resulting width of the bottom channel was 260 nm, with an under-cut of approximately 40 nm from the opening of the top channel (Fig. 1b). The sample was then treated with another plasma ashing step at 5 mBar for 15 s in order to remove possible LOR residue on the bottom of the channel and making the PMMA hydrophilic and thereby incapable of supporting motility. Finally, the sample was silanized, in a chemical vapor phase deposition (CVD) process (Bunk et al., 2005a; Sundberg et al., 2003), with trimethylchlorosilane (TMCS, > 97%, GC, Sigma-Aldrich, Sweden AB, Stockholm, Sweden) in a closed glass container inside a glove box, with sub-ppm levels of O_2 and H_2O. As a final step before the in vitro motility assay procedure, the sample was steamed in a deionized water bath for 30 s to wet the channels and remove possible air bubbles. The surfaces were rinsed in distilled water for 10 min prior to use. The above account describes the key steps in producing the first generation concentration device. The second-generation

concentration device was fabricated in a similar way but without any LOR layer (Fig. 4a).

### 2.2. Protein preparations and in vitro motility assays

Myosin II was purified from rabbit fast skeletal muscle (Sata et al., 1993) and then digested by α-chymotrypsin to yield HMM (Kron et al., 1991). Actin filaments were prepared from rabbit skeletal muscle (Pardee and Spudich, 1982) and fluorescently labeled with Alexa Fluor 488® phalloidin (APh) or tetramethylrhodamineisothiocyanate (TRITC)–phalloidin (RhPh; Molecular Probes Invitrogen, Eugene, OR) (Balaz and Mansson, 2005).

Flow cells were constructed from one cover-slip and one nanostructured chip on top with double-sided sticky tape as spacers. All solutions that were added to the flow cell were based on buffer A (1 mM $MgCl_2$, 10 mM 3-(N-morpholino)propanesulfonic acid MOPS, 0.1 mM K_2-ethylene glycol tetraacetic acid (EGTA), pH 7.4) and all proteins were diluted in buffer B (buffer A with 1 mM dithiothreitol (DTT) and 50 mM KCl). The flow cell was pre-incubated essentially as described previously (Kron et al., 1991; Sundberg et al., 2006b): (i) HMM (120 μg mL^{-1}) for 4 min, (ii) bovine serum albumin (BSA; 1 mg mL^{-1}) for 1 min, (iii) blocking actin (1 μM unlabeled sheared actin filaments with 1 mM MgATP) for 2 min. These pre-incubation steps were followed by (iv) wash with a50 assay solution (buffer A with 10 mM DTT, 1 mM MgATP, 35 mM KCl, ionic strength 50 mM) and (v) addition of actin filaments at 10 nM (second generation) or 100 nM (first generation). After an incubation period of 1 min, flow cells were washed with buffer B and (vi) incubated with rigor solution (r60) for initial observation in the microscope. The latter solution had the same composition as the a50 solution but without MgATP and with 45 mM instead of 35 mM KCl, giving an ionic strength 60 mM. An anti bleach mixture of 3 mg mL^{-1} glucose, 100 μg mL^{-1} glucose oxidase and 870 U mL^{-1} catalase was added. Soon after the recording was started, flow cells were (vii) incubated with a60 solution (r60 with 1 mM MgATP and an ATP re-generating system: 2.5 mM creatine phosphate and 3.5 U mL^{-1} creatine phosphokinase). For the second generation concentrator device the procedure was similar as described above, but the incubation step with block actin and subsequent washing steps (steps iii and iv) were omitted.

To demonstrate analyte concentration we rinsed the second generation device after previous use with (i) a130 solution (similar to a60 but with an ionic strength of 130 mM) and (ii) buffer B before incubation with (iii) 10 nM biotinylated APh labeled actin filaments for one minute. The flow cell was then rinsed with (iv) buffer B and, incubated with (v) TRITC–streptavidin (2 nM) for one minute. To block remaining sites on streptavidin and avoid cross-linking of filaments via streptavidin–biotin links, the flow cell was then rinsed with (vi) biotin (30 μM). Subsequently, (vii) buffer B was infused. Flow cells were then incubated with (viii) r60 solution and observed in the microscope before motility was induced by (ix) addition of a60 solution.

2.3. Data collection and analysis of in vitro motility assays

Fluorescently labeled actin filaments were observed using a Nikon Eclipse TE300 inverted fluorescence microscope (Nikon Corporation, Tokyo, Japan) equipped with a temperature-regulated Nikon (100× 1.4 NA) oil immersion objective and TRITC (Ex. 540/25, DM 565, and BA 605/25) and FITC (Ex. 465–495, DM 505, and BA 515–555) filter sets. A cooled Hammamtsu EMCCD camera (C9100-12) was used to record image sequences (Persson et al., 2010) which were then analyzed using algorithms developed in the MATLAB (Mathworks Inc., Natick, MA; Mansson and Tagerud, 2003). Image sequences were further analyzed using Image J (Rasband, W.S., ImageJ, U S National Institutes of Health, Bethesda,
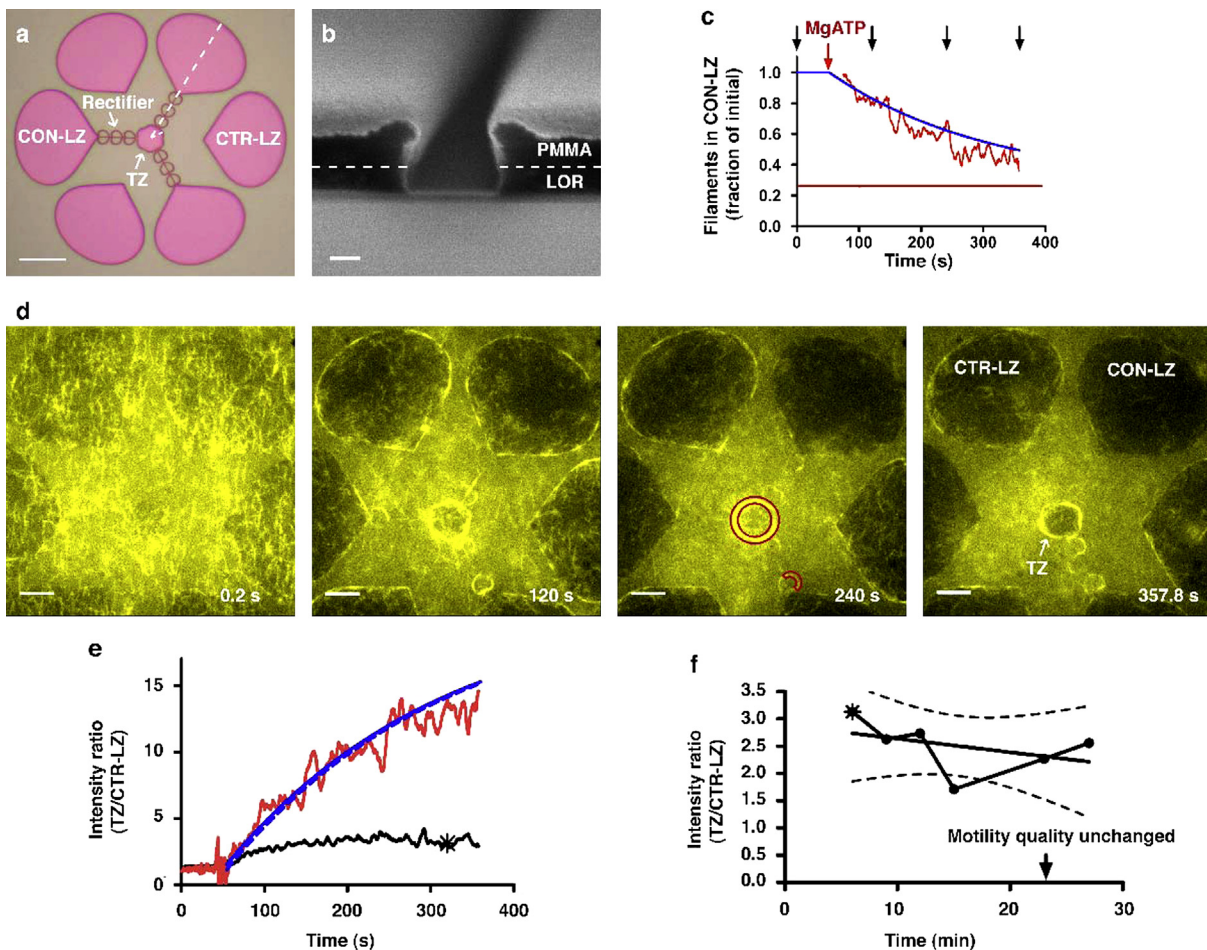
Fig. 1. Experiments using first generation concentrator device: (a) Design (resist mask): trapping zone (TZ), 3 control loading zones (CTR-LZ) and 3 loading zones connected to trapping zone (CON-LZ) via nanochannels. Pink: functional HMM. White dashed lines indicate symmetery lines delimiting areas for Monte-Carlo simulations (Supporting Methods; Fig. S1). Scale bar: 20 μm. (b) Scanning electron micrograph of nano-sized channel. Scale bar: 100 nm. (c) Ratio between background-subtracted intensities: CON-LZ/CTR-LZ vs. time. Red noisy curve: early after MgATP addition. Red straight line: steady-state. Blue: fraction of filaments in CON-LZ in Monte-Carlo simulations. (d) Fluorescence micrographs showing TRITC-phalloidin labeled actin filaments and autofluorescent LOR at times corresponding to black arrows in c. Before MgATP addition (0.2 s), actin filaments also bound to PMMA. Temperature: 22 °C. Image enhancement by histogram stretching. Scale bar: 10 μm. Red shapes: appropriate detector locations. (e) Filament accumulation on TZ according to Eq. (1) and c (same color code as c) or measured (black) from intensity ratio TZ/CTR-LZ. Star, same data point as star in f. Dashed blue line: Monte-Carlo model including delay due to transport along nano-sized track between CON-LZ and TZ and (f) intensity ratio TZ/CTR-LZ at steady-state, different times after MgATP addition. Similar temperature and motility quality (fraction of motile filaments [> 70%], velocity [∼4 μm/s]) as at $t=1$ min. Straight line: regression line with 95% confidence interval (dashed lines). (For interpretation of the references to color in this figure legend, the reader is referred to the web version of this article.)

Maryland, USA, ⟨http://imagej.nih.gov/ij/⟩, 1997–2012) by selecting the area of interest (trapping zone, connected loading zone or control loading zone, Fig. S1) followed by measurements of the mean intensity for each frame. The mean fluorescence intensities in the connected loading zone and trapping zone were first background subtracted followed by division with the mean background subtracted intensity of the control loading zone in the same frame (to correct for photobleaching). The background intensity levels in these analyses were obtained as the average intensity of seven filament free regions of interest observed 300 s after onset of illumination.

3. Results and discussion

3.1. First generation device

A biosensing principle that is unique to molecular motors and cytoskeletal filaments, is detection based on co-transportation of analytes and cytoskeletal filaments conjugated with antibodies or other recognition molecules (discussed in Korten et al. (2013);

Månsson et al. (2012b)). This approach is here enhanced by a concentration scheme for increased S/N ratio and automation. As a basis for later rational design we first tested a device were actin filaments were captured by HMM (pink; Fig. 1a) adsorbed to relatively large TMCS-derivatized loading zones (Bunk et al., 2005b; Sundberg et al., 2006b). Upon ATP addition, the filaments were transported from these zones along nano-sized channels (Fig. 1b) to a trapping zone (detector area). The guidance of actin filaments along channels is more challenging (Nitta et al., 2008; Sundberg et al., 2006b; Vikhorev et al., 2008a, 2008c) than for microtubules due to low flexural rigidity. We thus used nanostructuring (EBL) for fabrication of guiding channels to make them narrow enough to prevent filament U-turns. In addition we used three pairs of rectifiers (Hiratsuka et al., 2001; van den Heuvel et al., 2005; Vikhorev et al., 2008c) (total measured rectification 96%) along each channel (Fig. 1a,b). In view of the previously demonstrated similarity in motility quality for Rh–Ph labeled filaments and for filaments transporting antibody–antigen complexes (Kumar et al., 2012) the concentrator performance was studied quantitatively using Rh–Ph labeled filaments, for optimal image quality.

The background-subtracted fluorescence intensity ratio (Fig. 1c) between loading zones connected to trapping zones (CON-LZ; Fig. 1a) and control loading zones (CTR-LZ) without such connection, reports the approximate change in the number of filaments on the connected loading zones corrected for photobleaching, (see further Fig. S2). This ratio decreased (Fig. 1d, Movie S1) with an exponential time course that was well reproduced (Fig. 1c) by Monte-Carlo simulations for a similar geometry and filament sliding velocity (details below). The expected ratio between average filament density in the trapping zone at infinite time (at steady-state; C_{SS}^T) and at time 0 s (C_i) is given by (Supporting Information Results and Discussion):

$$\frac{C_{SS}^T}{C_i} \approx \frac{k_+ f}{(k_+ + k_-)}\left(\frac{A_L}{A_T} + 1\right) \tag{1}$$

Here, the quantities k_+ and k_- are rate constants of filament-transitions from the loading zone and trapping zone, respectively. Further, f is the fraction of motile filaments and A_L and A_T is the area of the connected loading zones and the trapping zone, respectively. For the experiment in Fig. 1, with 3 connected loading zones, $A_L/A_T \approx 3438$ μm^2/123 μm$^2 \approx 27.9$ and $k_+ f/(k_+ + k_-) \approx 0.7$ (1-fraction of filaments remaining in connected loading zones at steady-state; straight line in Fig. 1c). From Eq. (1) and the observed time course in Fig. 1c the number of filaments in the trapping zone is predicted to increase as indicated by the red line in Fig. 1e to a steady-state value about 20 times the initial value. This is about 10 times larger than the observed increase (2.4 ± 0.2 times; $n=5$; black line in Fig. 1e), a difference that we attribute to loss of filaments (Fig. S3) from the trapping zone at high filament densities. That similar detachment of filaments from the trapping zone did not occur at moderate and low filament densities is indicated by a nearly constant intensity ratio between trapping zone and control loading zone for > 20 min after attainment of steady-state (Fig. 1f).

The detachment and the associated deviation between experiments and simulations are likely to be seriously aggravated by the presence of blocking actin. The blocking actin filaments are not fluorescence labeled and added at about 1 μM prior to addition of fluorescence labeled actin filaments (added at nannomolar concentrations). The purpose is to block rigor HMM heads that may otherwise interfere with the transportation of fluorescent actin filaments but a large fraction of the blocking actin filaments are actually motile (Sundberg et al., 2006a) and will compete with fluorescent filaments for HMM binding sites. The competition is particularly severe when the filaments become enriched in the trapping zone, emphasizing the importance of omitting blocking actin when using nanostructured concentration devices. This is also done in the tests below.

The filament density distribution in the trapping zone was spatially non-uniform (Fig. 1d) with 2.7 ± 0.3 times (mean $\pm$ standard error of the mean [SEM]; $n=3$) higher filament density (from intensity data) within 1 μm from the trapping zone edge than at the center. Filaments also exhibited high local density in the semi-circular part of the rectifier structure. This suggests that the signal-to-noise ratio would be enhanced with detectors located in such regions (see highlighted red regions in Fig. 1d) and that the trapping zones may be modified to circular loops (see below).

3.2. Monte-Carlo simulations for rational concentrator design

For cytoskeletal filaments propelled by molecular motors on a surface without chemical or topographical patterns (flat surfaces) the instantaneous angular changes in sliding direction are expected to be the Gaussian with mean 0 rad and standard deviation, $SD = \sqrt{v_f \Delta t / L_P}$ where v_f is the sliding velocity, Δt is the time interval between subsequent updates in sliding direction and L_P is the filament persistence length (Duke et al., 1995; Nitta and Hess, 2005; Vikhorev et al., 2008a, 2008c). At walls, designed to guide approaching filaments with close to 100% probability (as used here), the random diffusion-like motion is prevented (Clemmens et al., 2003a, 2003b; Sundberg et al., 2006b; van den Heuvel et al., 2005) as the filaments are forced to follow the walls.

On the above grounds, we simulated the behavior of an ensemble of actin filaments in a concentrator device similar to that in Fig. 1 using a Monte-Carlo approach (Nitta et al., 2006, 2008). In the present study the simulations were implemented in the Matlab with the filament behavior at the walls treated as previously (Månsson et al., 2012a). Further details are given in the supporting information but it is of relevance to mention here that the loading zone shape was defined by a combination of an elliptical and triangular region (Fig. S1).

The validation of the Monte-Carlo simulation with respect to its capability to predict the time course of the concentration process (Fig. 1c) enables optimization of the concentrator design for speed without time consuming and expensive experiments. This is particularly important as such experiments also suffer from difficulties to follow rapid time courses. The Monte-Carlo simulations showed that the time course of the concentration process was approximately exponential (Figs. 1c and 3) with a half-time inversely proportional to the sliding velocity (Fig. 2e) and directly proportional to loading zone area (Fig. 2f). Further, a transition from nearly circular to triangular loading zones reduces the half-time by almost one order of magnitude (Fig. 3b). The simulated effects of sliding velocity and loading zone area on the concentration half-time were expected if the filaments largely executed motor driven diffusion (Vikhorev et al., 2008c). Thus, with a characteristic length scale r and a diffusion constant for motor driven diffusion, D, the characteristic time, t_{char}, is given by $t_{char} = \langle r^2 \rangle / 4D$ where $D \approx v_f L_p$ (Vikhorev et al., 2008c). Consequently, t_{char} would be proportional to the area and inversely proportional to the velocity and persistence length in accordance with the simulation results (Fig. 2e,f). The increased rate with a more triangular shape of the loading zone, on the other hand, accords with increased degree of filament edge-tracing (Bunk, 2005; Månsson et al., 2012a) toward the outlet opening, i.e. an increased ratio of ballistic to diffusion like transport (see also Nitta and Hess, 2012).

3.3. Second generation concentrator device optimized for speed and enrichment

On basis of the simulation results, Eq. (1) and further considerations above we arrived at the optimized device design in Fig. 4a, characterized by smaller loading zones (each with ~ 270 μm^2 area) with largely triangular shape and a circular loop (Bunk, 2005; Sundberg et al., 2006b) as detection area. The number of loading zones was increased to maintain high total area (A_L, Eq. (1)) and the detection area was reduced to $A_T \approx 8.5$ μm^2.

Upon ATP-addition, at 26–27 °C, the fluorescence intensity on the connected loading zone decreased (due to movement of actin filaments into the detection area) with a half-time of 30 and 40 s (Fig. 4) in two different experiments. This is considerably longer than the half-time in the range 10–14 s (95% confidence interval [CI]; degrees of freedom: 4) predicted by the Monte-Carlo simulations for the average sliding velocity (mean $\pm$ SEM: 6.79 ± 0.18 μm/s; $n=90$) measured from smoothly sliding filaments during the first minutes after ATP infusion. We attribute this discrepancy to average filament velocities and path persistence lengths that are lower in the experiments than the values of 6 μm/s (see above) and 10 μm (Vikhorev et al., 2008b) used in the simulations. These lower values may be due to rigor myosin heads causing temporary stops of a fraction of the filaments or pinning of sliding filaments causing
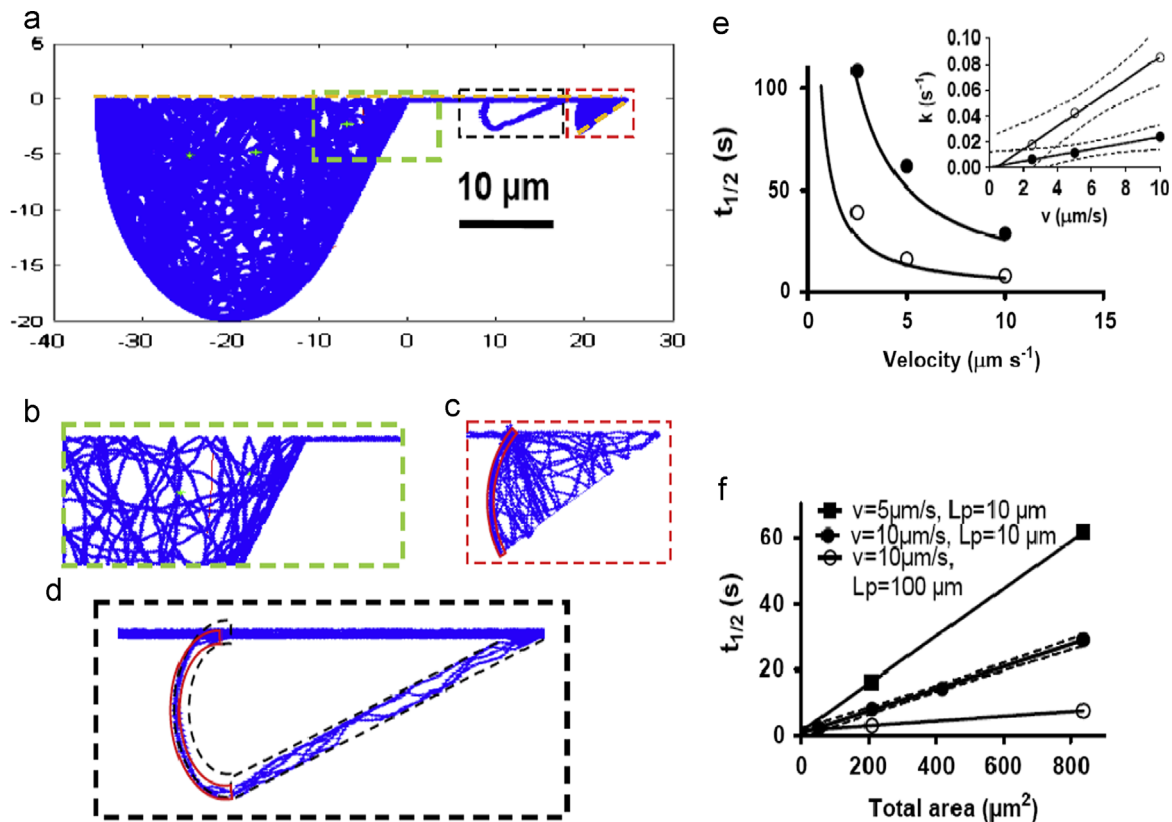
Fig. 2. Monte Carlo simulations of concentrator device performance: (a) Example paths (3 filaments; velocity, 10 μm/s; 120 s) in Monte-Carlo simulations of relevant regions in a concentrator device similar to that in Fig. 1a but with 6 symmetrically connected loading zones. Modeled filament paths reflected in symmetry lines indicated by dashed orange lines corresponding to white dashed lines in Fig. 1a. (b–d) Close-up views of areas delimited by dashed rectangles in a. Red shapes: suitable detector locations. (e) Simulated half-times ($t_{1/2}$) of loading-zone emptying vs. velocity (loading zone area: open symbols, 209 μm^2; filled symbols, 836 μm^2). Inset: rate constants (ln $2/t_{1/2}$) vs. velocity. Persistence length 10 μm. (f) Simulated half-times ($t_{1/2}$) vs. area of loading zones for different velocities (v_f) and filament persistence lengths (L_P). Lines in (e) and (f) are obtained by linear or non-linear regression analysis. (For interpretation of the references to color in this figure legend, the reader is referred to the web version of this article.)
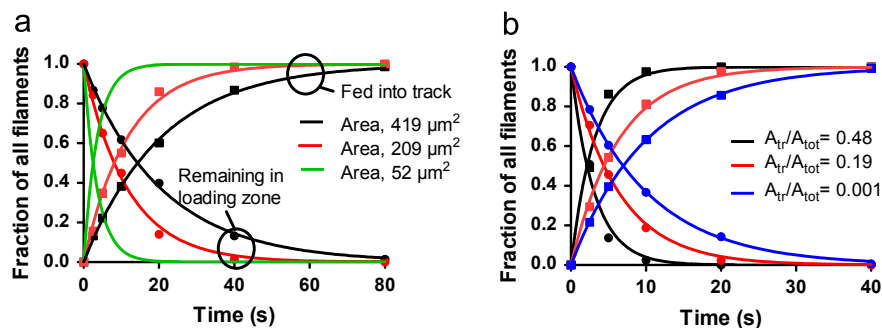

Fig. 3. Simulated time courses of emptying of loading zone and feeding into track to central trapping zone. Filled symbols, simulated data using the Monte-Carlo approach. Lines, non-linear regression fits to single exponentials: (a) Effects of loading zone area and (b) effects of the part of the loading zone area that is triangular (A_{tr}; cf. Fig. S4) relative to total area of loading zone (A_{tot}; similar for all cases). Simulated velocity, 10 μm s^{-1}.

sharp turns that reduce the apparent path persistence length (Vikhorev et al., 2008c). The fraction of such heads is likely to be more substantial in the experiment in Fig. 4 compared to that in Fig. 1 due to the use of blocking actin in the latter but not in the former.

The fluorescence intensity due to filaments accumulating on the detector zone after ATP addition (Fig. 4b) indicated a more than 20-fold increase in filament density relative to the loading zone (Fig. 4d). This may be compared to a more than 90-fold increase predicted by Eq. (1) on basis of total loading and trapping zone areas, with $>60\%$ of the filaments motile and $k_+/(k_++k_-)$ >0.8 (approximated from experimental data). The observed discrepancy is attributed to loss of filaments from the trapping zone into solution (Fig. S4). Whereas the ratio $k_+/(k_++k_-)$ could be made close to 1 by adding rectifier structures (see Fig. 1a) this is not meaningful until escape into solution is eliminated. A major reason for this type of escape is the very extensive accumulation of filaments in the trapping zone loop (Månsson et al., 2012a) leaving only few myosin heads for binding to each actin filament (see detailed analysis below). The inter-filament competition for motors is particularly problematic with a non-processive motor such as myosin II. On the other hand, the fact that the motor is non-processive is also the basis for the high speed and the fast concentration. Therefore, any intervention directed to the
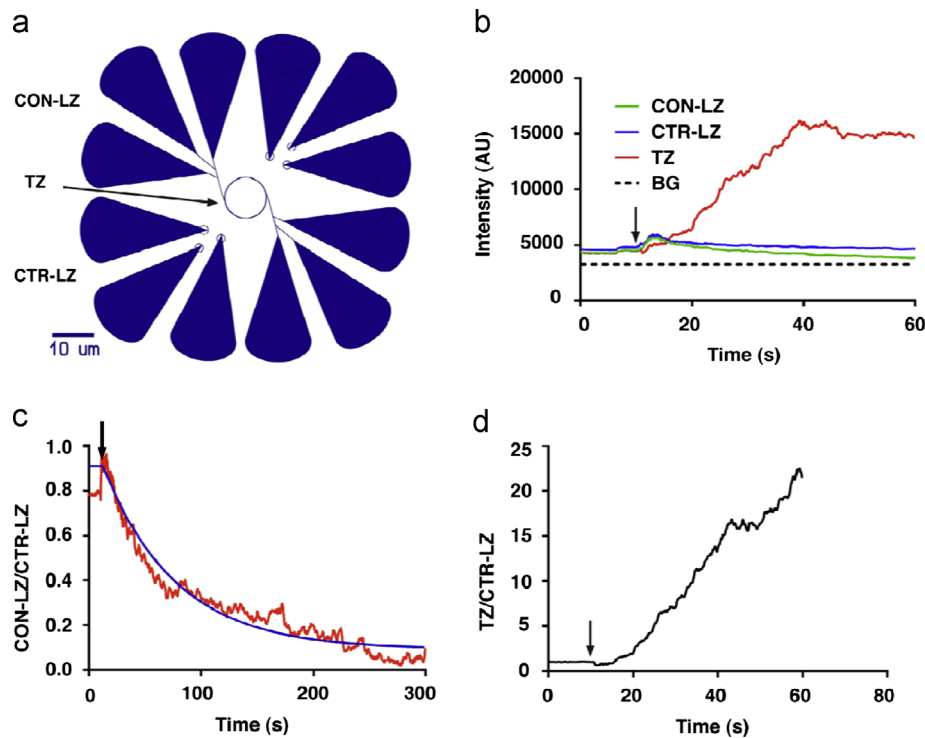
Fig. 4. Second generation concentrator device: (a) Device design. Blue areas with TMCS and functional HMM. White areas with PMMA and no HMM function. Motility supporting loops at sharp peak of CTR-LZ to prevent filament escape into solution. Six connected loading zones, each with area ≈260 μm^2. (b) Time courses (raw data) for changes in average fluorescence intensities of APh-labeled filaments in TZ (red), CTR-LZ (blue) and CON-LZ (green). Black dashed line: background fluorescence level. Arrow: ATP infusion (same in c and d), (c) ratio between average fluorescence intensities on CON-LZ and CTR-LZ vs. time. Blue curve: single exponential equation (with time delay) fitted to the data by non-linear regression, giving decay half-time of 42 s (95% CI: 40.2–42.3 s; degrees of freedom: 1427) and (d) ratio of background-subtracted TZ and CTR-LZ intensities normalized to the value before ATP-infusion. (For interpretation of the references to color in this figure legend, the reader is referred to the web version of this article.)

actomyosin interaction and aiming to make the motor more processive would also be expected to reduce the velocity and concentration rate. Instead, it seems important to use overhanging channel roofs (Bunk et al., 2005a) partly implemented in the first-generation device. However, the second generation device did not use such roofs, since we omitted the LOR resist layer to appreciably reduce autofluorescence and thereby facilitate image analysis. Alternatively, the entire trapping zone may be covered with a roof (Lin et al., 2008). Another useful approach may be to reduce the number of actin filaments on the loading zone by using a magnetic pre-concentration step (also used in e.g. bio-barcode method (Nam et al., 2003)). Here, the analyte would first be captured on magnetic nanoparticles with specific antibodies followed by cross-linking to actin filaments with antibodies against another part of the analyte. Next, only actin filaments cross-linked to a magnetic particle will be guided toward the surface using a magnetic field. If magnetic nanoparticles are used, myosin driven transport would be little affected (Persson et al., 2013), particularly at low analyte binding.

It is of interest to estimate the maximum possible packing density for actin filaments in the detector area. For instance, with a trapping zone as in Fig. 4 (radius=5 μm), a channel width of 270 nm and an actin filament diameter of 10 nm, the maximum possible length of the trapped actin filaments would be $2 \times \pi \times 5 \mu m \times 270 nm/10 nm = 848 \mu m$. If the average filament length is in the range 2–5 μm this would correspond to 170–420 filaments, completely covering the surface. However, if space is required for the myosin heads along the side of an actin filament, as indicated by electron microscopy images of actin filaments with bound HMM (Katayama, 1998), then each filament is more likely to occupy a width of about 30 nm. This would give room for only nine filaments side by side (compared to a maximum of four

observed; from intensity data) corresponding to a total filament length of 283 μm, i.e. 57–141 filaments. Importantly, the theoretical concentration maximum according to Eq. (1) can only be reached if the initial number of motile filaments on the loading zone is smaller than the maximum number of filaments that can be packed into the trapping zone. Further, the degree of concentration of analyte in the detector area will also be appreciably reduced if only a fraction of the motile filaments have bound analyte. This would be the case with low analyte concentration in solution if no magnetic pre-concentration is used, again emphasizing the importance of such a step.

At relatively high, nanomolar analyte concentrations, on the other hand, magnetic pre-separation is not required. Accordingly, we show effective concentration and detection of a model analyte (fluorescent streptavidin) at nanomolar concentration. A solution with streptavidin (2 nM) was first added to biotinylated actin filaments bound to HMM on the loading zone surface (incubation for 1 min). This was followed by a number of rinsing steps before ATP was infused. Then, a signal from the detector area, clearly distinguished from the background noise, was obtained within seconds (Fig. 5). We expect that most rinsing steps are omitted in a real device operation, leading to a total time from streptavidin infusion to detection corresponding to less than 2 min. In this experiment, streptavidin was captured from the solution in a flow cell of 100 μm height. The area, A, parallel to the flow-cell surface where diffusion equilibration occurs within time t is approximated as $A = \pi 4Dt$ where $D \approx 50 \mu m^2 s^{-1}$ is the diffusion coefficient of streptavidin (Janmey et al., 1986). Now inserting, $t = 60$ s we obtain $A \approx 38,000 \mu m^2$ corresponding to a volume of 4 nl over the height of the flow cell. Thus, the described device achieves, within 2 min, detection of attomole quantities of streptavidin corresponding to nM concentrations in nanoliter volumes.
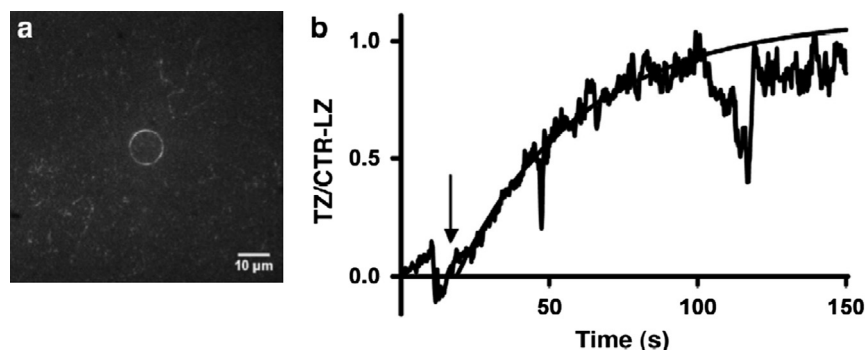
Fig. 5. Motor-driven concentration of streptavidin: (a) TRITC streptavidin fluorescence localized mainly in central trapping zone approximately 60 s after addition of ATP. Note minimal fluorescence on connected loading zones (located as in Fig. 4a) and also low fluorescence on control-loading zone (Fig. 4a), due to photo-bleaching and (b) background-subtracted time course of increase in TRITC-streptavidin fluorescence intensity on trapping zone following (i) incubation with biotinylated actin filaments on loading zone with 2 nM streptavidin for 1 min and (ii) addition of ATP containing assay solution (at arrow). Full line represents exponential curve with a time delay (half-life: 30 s; 95% CI: 27–33 s; degrees of freedom: 498) fitted to the data by non-linear regression for times < 100 s.

3.4. Comparison with existing methods

It is of interest to relate the detection approach in Fig. 5 to standard immunometric methods (Wild, 2013) where recognition molecules such as antibodies are immobilized on a solid support. In this case, analytes captured by the immobilized antibodies are often detected by a second antibody, specific to another epitope of the analyte than the surface immobilized antibodies. This second antibody may be tagged with a fluorophore or an enzyme catalyzing the formation of a colored product (enzyme-linked immunosorbent assay; ELISA). Before the actual detection step a rinsing step removes unbound tagged antibodies. As an alternative to the use of a tagged antibody, all proteins in the sample may be fluorescence labeled, e.g. using standard lysine linking chemistry (Wingren et al., 2007) before applying the sample to the surface adsorbed recognition molecules (cf. our detection of fluorescent streptavidin). A potential problem with the standard methods is false detection of an analyte due to non-specific background fluorescence e.g. due to free fluorophore or detection antibody. Highly miniaturized sensors (nanosensors) partly circumvent this problem but the small areas severely limits diffusion to the detector (Sheehan and Whitman, 2005). This transport problem is overcome by motor driven transport (Katira and Hess, 2010b). In this connection, the use of actomyosin allows a significantly higher level of miniaturization compared to previous microtubule-kinesin based devices. This feature is facilitated by the low flexural rigidity of the actin filaments. The immobilization of the antibodies to the actin filaments also has other advantages. First, the actin filament is a more benign surface for antibody immobilization (Kumar et al., 2012) than e.g. a non-biological polymer surface. Second, the immobilization of the recognition molecule to actin filaments separates the binding sites of analytes from the detection site. Thus, in the initial absence of ATP the actin filaments with recognition molecules are bound only to the large loading zone areas, as they do not readily diffuse into the detector areas. When an analyte reaches a loading zone by diffusion it will execute effective diffusional search close to the surface and is likely to be swiftly captured by the recognition molecules even if the surface is not completely filled with antibody conjugated filaments (Berg and Purcell, 1977; Katira and Hess, 2010a). Next, when ATP is added, the transport of actin filaments from the loading zone to the detection zone is very rapid. In this way, the motor driven device takes advantage of both a large initial capture area and a small detector area for high signal-to-noise ratio. Finally, the close temporal correlation between ATP-addition and appearance of fluorescence at the detector site is a unique sensor mechanism that appreciably increases specificity of motor driven devices.

With regard to rate of detection, it is of interest to note that the characteristic time for the amplification step attributed to optimized motor driven enrichment (< 1 min) compares favorably to the corresponding time (30 min) in a high-sensitivity bio-barcode assay (Georganopoulou et al., 2005; Nam et al., 2003). This fast time scale, by itself, increases detection accuracy because a fast time transient removes masking by background drift. Additionally, fast device performance minimizes any problems with unstable biological components and also limits effects of complex fluid environments, e.g. blood serum (Korten et al., 2013). The use of the actomyosin system could be expanded to larger cargoes (e.g. microvesicles, bacteria etc.) by using actin bundles (Takatsuki et al., 2010, 2011) without sacrificing the high sliding speed. On the other hand, the use of actin filaments is sufficient for protein analytes (Kumar et al., 2012; Persson et al., 2013a) and would be advantageous for miniaturization purposes.

While awaiting important confirming tests on real samples, the described device holds considerable promise for use in point-of-care diagnostics. This is due to the extreme miniaturization, the independence from microfluidic pumping and the recent demonstration of actomyosin storage in an ordinary household freezer for months (Albet-Torres and Mansson, 2011) as well as the emergence of drugs that extend actomyosin shelf-life (Radke et al., 2012). Indeed the shelf-life (Albet-Torres and Mansson, 2011; Grove et al., 2005) for actomyosin based devices seems comparable to commercially available point of care test methods for e.g. the inflammation marker C-reactive protein, frequently tested in clinical practice. It is therefore also of interest to note that the relevant plasma concentration range (nM to μM) (Pepys and Hirschfield, 2003) for this macromolecule is within reach for rapid detection using our concentrator device.

4. Conclusions

We have demonstrated rapid nanoseparation with unprecedented miniaturization (device area: ∼0.01 mm^2) using an actomyosin driven nanoseparation device. Several key improvements can be summarized from these results. The smaller device features, and the associated potential for device miniaturization compared to previously reported molecular-motor based devices was made possible by the low flexural rigidity of the actomyosin system. The fast and specific transport of analyte molecules by the motor system, from large capture areas to smaller concentration regions, allows for reliable and sensitive detection, while reducing the risk of erroneous detection. Limitations include the risk of detachment of filaments from the concentration area upon dense

accumulation of filaments. This can be addressed by using a ceiling above the detection area, which will also aid in improving the level of concentration and detection. In a real-world application of the concetrator device, integration of a detector into the detection region, e.g. optical (Bunk, 2005; Lard et al., 2013) magnetoresistive (Schotter et al., 2004) or amperometric (Gao et al., 2011), will allow automatic read-out. In a complete point-of-care diagnostics workflow, the concentrator device would most favorably be combined with initial capture of analyte on magnetic particles for magnetic pre-separation as in other high-sensitivity detection methods (Nam et al., 2003). Such separation would also help alleviate deleterious effects of body fluids on actomyosin function (Korten et al., 2013), a critical step toward the use of this method with real samples, such as blood serum.

Acknowledgments

Appendix A. Supplementary Information

Supplementary data associated with this article can be found in the online version at http://dx.doi.org/10.1016/j.bios.2013.03.071.

References

Albet-Torres, N., Mansson, A., 2011. Langmuir 27 (11), 7108–7112.
Ashikari, Y., Shitaka, Y., Fujita, K., Kojima, H., Oiwa, K., Sakaue, H., Takahagi, T., Suzuki, H., 2012. Japanese Journal of Applied Physics 51 (2), 02BL03.
Bachand, G.D., Rivera, S.B., Carroll-Portillo, A., Hess, H., Bachand, M., 2006. Small 2 (3), 381–385.
Balaz, M., Mansson, A., 2005. Analytical Biochemistry 338 (2), 224–236.
Berg, H.C., Purcell, E.M., 1977. Biophysical Journal 20 (2), 193–219.
Brunner, C., Wahnes, C., Vogel, V., 2007. Lab Chip 7 (10), 1263–1271.
Bunk, R., 2005. Solid State Physics,. Lund Institute of Technology, Lund University, Lund.
Bunk, R., Sundberg, M., Mansson, A., Nicholls, I.A., Omling, P., Tagerud, S., Montelius, L., 2005a. Nanotechnology 16 (6), 710–717.
Bunk, R., Sundberg, M., Nicholls, I.A., Omling, P., Tågerud, S., Månsson, A., Montelius, L., 2005b. Nanotechnology 16, 710–717.
Byun, K.E., Kim, M.G., Chase, P.B., Hong, S.H., 2007. Langmuir 23 (19), 9535–9539.
Clemmens, J., Hess, H., Howard, J., Vogel, V., 2003a. Langmuir 19 (5), 1738–1744.
Clemmens, J., Hess, H., Lipscomb, R., Hanein, Y., Bohringer, K.F., Matzke, C.M., Bachand, G.D., Bunker, B.C., Vogel, V., 2003b. Langmuir 19 (26), 10967–10974.
Duke, T., Holy, T.E., Leibler, S., 1995. Physical Review Letters 74 (2), 330–333.
Fischer, T., Agarwal, A., Hess, H., 2009. Nature Nanotechnology 4 (3), 162–166.
Gao, W., Dong, H., Lei, J., Ji, H., Ju, H., 2011. Chemical Communications (Cambridge) 47 (18), 5220–5222.
Georganopoulou, D.G., Chang, L., Nam, J.M., Thaxton, C.S., Mufson, E.J., Klein, W.L., Mirkin, C.A., 2005. Proceedings of the National Academy of Sciences 102 (7), 2273–2276.
Giljohann, D.A., Mirkin, C.A., 2009. Nature 462 (7272), 461–464.
Grove, T.J., Puckett, K.A., Brunet, N.M., Mihajlovic, G., McFadden, L.A., Peng, X.O., von Molnar, S., Moerland, T.S., Chase, P.B., 2005. IEEE Transactions on Advanced Packaging 28 (4), 556–563.
Hess, H., Clemmens, J., Qin, D., Howard, J., Vogel, V., 2001. Nano Letters 1 (5), 235–239.
Hiratsuka, Y., Tada, T., Oiwa, K., Kanayama, T., Uyeda, T.Q.P., 2001. Biophysical Journal 81 (3), 1555–1561.
Janmey, P.A., Peetermans, J., Zaner, K.S., Stossel, T.P., Tanaka, T., 1986. Journal of Biological Chemistry 261 (18), 8357–8362.
Jokerst, J.V., Jacobson, J.W., Bhagwandin, B.D., Floriano, P.N., Christodoulides, N., McDevitt, J.T., 2010. Analytical Chemistry 82 (5), 1571–1579.
Katayama, E., 1998. Journal of Molecular Biology 278 (2), 349–367.
Katira, P., Hess, H., 2010a. Nano Letters 10 (2), 567–572.
Katira, P., Hess, H., 2010b. Nano Letters 10 (2), 567–572.

Korten, S., Albet-Torres, N., Paderi, F., Ten Siethoff, L., Diez, S., Korten, T., Te Kronnie, G., Mansson, A., 2013. Lab Chip 13 (5), 866–876.
Korten, T., Månsson, A., Diez, S., 2010. Current Opinion in Biotechnology 21, 477–488.
Kron, S.J., Toyoshima, Y.Y., Uyeda, T.Q., Spudich, J.A., 1991. Methods Enzymology 196, 399–416.
Kumar, S., ten Siethoff, L., Persson, M., Lard, M., te Kronnie, G., Linke, H., Månsson, A., 2012. PLoS ONE 7 (10), e46298.
Lard, M., Siethoff, L.T., Mansson, A., Linke, H., 2013. Scientific Reports 3, 1092.
Lee, K.B., Kim, E.Y., Mirkin, C.A., Wolinsky, S.M., 2004. Nano Letters 4 (10), 1869–1872.
Lin, C.T., Kao, M.T., Kurabayashi, K., Meyhofer, E., 2008. Nano Letters 8 (4), 1041–1046.
Mansson, A., Tagerud, S., 2003. Analytical Biochemistry 314 (2), 281–293.
Mulvaney, S.P., Myers, K.M., Sheehan, P.E., Whitman, L.J., 2009. Biosensors and Bioelectronics 24 (5), 1109–1115.
Månsson, A., Bunk, R., Sundberg, M., Montelius, L., 2012a. Journal of Biomedicine and Biotechnology 2012, 647265.
Månsson, A., Kumar, S., Lard, M., Ten Siethoff, L., Persson, M., Albet-Torres, N., Te Kronnie, G., Linke, H., 2012b. Journal of Muscle Research and Cell Motility 33, 279.
Månsson, A., Sundberg, M., Balaz, M., Bunk, R., Nicholls, I.A., Omling, P., Tågerud, S., Montelius, L., 2004. Biochemical and Biophysical Research Communications 314 (2), 529–534.
Månsson, A., Sundberg, M., Bunk, R., Balaz, M., Nicholls, I.A., Omling, P., Tegenfeldt, J.O., Tågerud, S., Montelius, L., 2005. IEEE Transactions on Advanced Packaging 28 (4), 547–555.
Nam, J.M., Thaxton, C.S., Mirkin, C.A., 2003. Science 301 (5641), 1884–1886.
Ng, A.H., Uddayasankar, U., Wheeler, A.R., 2010. Analytical and Bioanalytical Chemistry 397 (3), 991–1007.
Nicolau, D.V., Suzuki, H., Mashiko, S., Taguchi, T., Yoshikawa, S., 1999. Biophysical Journal 77 (2), 1126–1134.
Nitta, T., Hess, H., 2005. Nano Letters 5 (7), 1337–1342.
Nitta, T., Hess, H., Cellular and Molecular Bioengineering 6 (1), 2013, 109–115.
Nitta, T., Tanahashi, A., Hirano, M., Hess, H., 2006. Lab Chip 6 (7), 881–885.
Nitta, T., Tanahashi, A., Obara, Y., Hirano, M., Razumova, M., Regnier, M., Hess, H., 2008. Nano Letters 8 (8), 2305–2309.
Pardee, J.D., Spudich, J.A., 1982. Methods in Cell Biology 24, 271–289.
Pepys, M.B., Hirschfield, G.M., 2003. Journal of Clinical Investigation 111 (12), 1805–1812.
Persson, M., Albet-Torres, N., Ionov, L., Sundberg, M., Hook, F., Diez, S., Mansson, A., Balaz, M., 2010. Langmuir 26 (12), 9927–9936.
Persson, M., Gullberg, M., Tolf, C., Lindberg, A.M., Mansson, A., Kocer, A., 2013. PloS ONE 8 (2), e55931.
Radke, M.B., Taft, M.H., Preller, N., Heissler, S.H., Steinke, N., Manstein, D.J., 2012. Biophysical Journal 102 (3, S1), 354a.
Ramachandran, S., Ernst, K.H., Bachand, G.D., Vogel, V., Hess, H., 2006. Small 2 (3), 330–334.
Rissin, D.M., Kan, C.W., Campbell, T.G., Howes, S.C., Fournier, D.R., Song, L., Piech, T., Patel, P.P., Chang, L., Rivnak, A.J., Ferrell, E.P., Randall, J.D., Provuncher, G.K., Walt, D.R., Duffy, D.C., 2010. Nature Biotechnology 28 (6), 595–599.
Sata, M., Sugiura, S., Yamashita, H., Momomura, S., Serizawa, T., 1993. Circulation Research 73 (4), 696–704.
Schotter, J., Kamp, P.B., Becker, A., Puhler, A., Reiss, G., Bruckl, H., 2004. Biosensors and Bioelectronics 19 (10), 1149–1156.
Sheehan, P.E., Whitman, L.J., 2005. Nano Letters 5 (4), 803–807.
Sundberg, M., Balaz, M., Bunk, R., Rosengren-Holmberg, J.P., Montelius, L., Nicholls, I.A., Omling, P., Tågerud, S., Månsson, A., 2006a. Langmuir 22 (17), 7302–7312.
Sundberg, M., Bunk, R., Albet-Torres, N., Kvennefors, A., Persson, F., Montelius, L., Nicholls, I.A., Ghatnekar-Nilsson, S., Omling, P., Tagerud, S., Mansson, A., 2006b. Langmuir 22 (17), 7286–7295.
Sundberg, M., Rosengren, J.P., Bunk, R., Lindahl, J., Nicholls, I.A., Tagerud, S., Omling, P., Montelius, L., Mansson, A., 2003. Analytical Biochemistry 323 (1), 127–138.
Suzuki, H., Yamada, A., Oiwa, K., Nakayama, H., Mashiko, S., 1997. Biophysical Journal 72 (5), 1997–2001.
Takatsuki, H., Rice, K.M., Asano, S., Day, B.S., Hino, M., Oiwa, K., Ishikawa, R., Hiratsuka, Y., Uyeda, T.Q., Kohama, K., Blough, E.R., 2010. Small 6 (3), 452–457.
Takatsuki, H., Tanaka, H., Rice, K.M., Kolli, M.B., Nalabotu, S.K., Kohama, K., Famouri, P., Blough, E.R., 2011. Nanotechnology 22 (24), 245101.
Vikhorev, P.G., Vikhoreva, N.N., Mansson, A., 2008a. Biophysical Journal 95 (12), 5809–5819.
Vikhorev, P.G., Vikhoreva, N.N., Mansson, A., 2008b. Biophysical Journal 95 (12), 5809–5819.
Vikhorev, P.G., Vikhoreva, N.N., Sundberg, M., Balaz, M., Albet-Torres, N., Bunk, R., Kvennefors, A., Liljesson, K., Nicholls, I.A., Nilsson, L., Omling, P., Tagerud, S., Montelius, L., Mansson, A., 2008c. Langmuir 24 (23), 13509–13517.
van den Heuvel, M.G.L., Butcher, C.T., Smeets, R.M.M., Diez, S., Dekker, C., 2005. Nano Letters 5 (6), 1117–1122.
Whitesides, G.M., 2006. Nature 442 (7101), 368–373.
Wild, D., 2013. The Immunoassay Handbook, 4th ed. Elsevier, Oxford.
Wingren, C., Ingvarsson, J., Dexlin, L., Szul, D., Borrebaeck, C.A., 2007. Proteomics 7 (17), 3055–3065.
Zhang, C.Y., Yeh, H.C., Kuroki, M.T., Wang, T.H., 2005a. Nature Materials 4 (11), 826–831.
Zheng, G., Patolsky, F., Cui, Y., Wang, W.U., Lieber, C.M., 2005b. Nature Biotechnology 23 (10), 1294–1301.